



Fundamental Electrochemical Insights of Vertically Aligned Carbon Nanofiber Architecture as a Catalyst Support for ORR

Ayyappan Elangovan, ¹ Jiayi Xu, ² Emery Brown, 1 Bin Liu, ² and Jun Li^{1,*,z}

¹Department of Chemistry, Kansas State University, Manhattan, Kansas 66506, United States of America
²Tim Taylor Department of Chemical Engineering, Kansas State University, Manhattan, Kansas, 66506, United States of America

Three-dimensionally (3D) architectured carbon supports have received great attention for fuel cell catalysts. However, the complicated structure makes the assessment of catalytic properties difficult using the conventional rotating disk electrode (RDE) method. This paper reports a systematic study on oxygen reduction reaction (ORR) with ion-beam sputtered Pt catalyst (at Pt loadings of 6.5–43 μg cm⁻²) on a vertically aligned carbon nanofiber (VACNF) array, consisting of conically stacked graphitic microstructures. The RDE studies reveal that thick 3D architecture of VACNFs exhibits enhanced limiting current density that deviates from the Levich equation for conventional thin-film catalysts. Nevertheless, useful information can be derived from RDE experiments with such systems. Molecular models representing VACNFs have been constructed to explore their capacity as catalyst supports for ORR. Platinum atoms form strong bonds at the open graphitic edges in VACNF, corroborating the role of VACNF in stabilizing Pt. Density Functional Theory (DFT) calculations further elucidate the two-electron and four-electron ORR pathways on the bare VACNF and Pt/VACNF catalysts, respectively. Furthermore, the Pt/VACNF catalysts show enhanced tolerance to methanol oxidation and a higher ability to recover from carbon monoxide poisoning in comparison to the benchmark Pt/C catalysts. These results provide critical insights for developing future high-performance electrocatalyst supports.

© 2020 The Electrochemical Society ("ECS"). Published on behalf of ECS by IOP Publishing Limited. [DOI: 10.1149/1945-7111/ab86c1]

Manuscript submitted February 5, 2020; revised manuscript received March 17, 2020. Published April 15, 2020.

Supplementary material for this article is available online

Low-temperature fuel cells (LTFCs) are attractive environmentally friendly alternatives to fossil fuel powered devices. 1-3 It directly converts oxygen and fuels into H₂O at moderate temperatures to release electrical energy. Even though the overall reaction is thermodynamically favored, the sluggish kinetics leads to the high electrochemical overpotential and low power density.² To enable broader impacts, the power density and durability of LTFCs need to be significantly improved and the cost needs to be reduced. Highly efficient electrocatalysts are key to achieving these goals. Particularly, the electrocatalytic oxygen reduction reaction (ORR) is one of the important reactions occurring in LTFCs.^{2,4} ORR proceeds by a direct four-electron (4-e⁻) reduction pathway to form H₂O (in acidic media) or OH⁻ (in alkaline media), or by a less efficient two-step two-electron (2-e⁻) reduction pathway involving the formation of corrosive intermediate species H2O2 (in acidic media) or $\mathrm{HO_2}^-$ (in alkaline media). $^{2-5}$ Platinum (Pt) nanoparticles (NPs) supported on Vulcan carbon, denoted as Pt/C, is the most effective ORR catalyst.^{2,4-6} However, the high cost and limited supply of Pt poses severe challenges for broader applications. In addition, the current Pt/C catalyst suffers from poor durability, CO poisoning, and methanol crossover reactions (in direct methanol fuel cells (DMFC)—a type of LTFC). ^{7–9} As a result, there is a strong demand to improve these properties. ^{2,3,10,11} This study focuses on exploring vertically aligned carbon nanofiber (VACNF) arrays as unique carbon-based catalyst support for Pt catalyst, with an emphasis on understanding its fundamental electrochemical properties in ORR using a rotating disk electrode (RDE) and its capability in improving Pt catalyst's tolerance to methanol crossover.

Vulcan carbon support in commercial Pt/C catalysts is so far quite successful. However, in the presence of oxygen at high electrode potentials, carbon corrosion occurs, leading to the detachment of Pt NPs from the carbon support and decline in fuel cell performance. ^{12–14} One of the approaches in solving these issues is to develop highly graphitic carbon materials as novel catalyst supports, such as graphene, ^{15–17} carbon nanotubes (CNTs), ^{18,19} carbon nanofibers (CNFs)^{20–22} and carbon NPs. ²³ These carbon materials exhibit higher chemical stability, high specific surface area, large structural

variety, tailorable surface chemistry, wide potential window, and high electrical conductivity, 19,24 which can reduce carbon corrosion and improve the durability of Pt NPs. Some studies indicated that Pt deposited on CNT or CNF supports also show higher CO tolerance. 25,26 In most studies, these CNT or CNF supports are in the form of randomly stacked networks. A few studies explored vertically aligned organic whiskers as catalysts support in so-called nanostructured thin-film (NSTF) catalysts. 27-29 Such vertically aligned structures allow the deposition of a low Pt mass (at $\sim\!\!0.1\text{--}0.22\,\mathrm{mg~cm^{-2}})$ via simple ion sputtering, $^{27\text{--}29}$ which has been found to present higher activity than the commercial Pt/C catalysts. Tian et al.³⁰ further explored vertically aligned CNTs sputtered with $\sim 35 \,\mu\mathrm{g}\,\mathrm{cm}^{-2}$ Pt in membrane electrode assemblies (MEAs) and the hydrogen fuel cell made of such MEAs matched the performance of the Pt/C catalyst with 10 times of Pt loading. In another direction, Gong et al.⁷ reported that vertically aligned nitrogen-doped CNT arrays can serve as a metal-free catalyst with superior catalytic activities.

While the above results are encouraging, it still lacks a good understanding of the fundamental electrochemical properties of such 3D electrodes in ORR. This is challenging because the large thickness and the porous 3D structure are substantially different from the conventional thin-film RDE electrodes (<200 nm) in ORR studies. It is noteworthy that voltammetry measurements with RDE are an essential technique for evaluating ORR electrocatalysts due to the low O_2 solubility in electrolytes ($\sim 1.2 \text{ mM}$) and sluggish kinetics. The well-defined hydrodynamic conditions based on the Levich equation enable deconvolution of mass transport and kinetic effects and thus allow determination of the electrochemical kinetics and ORR mechanisms.³¹ These cannot be achieved with other electrochemical techniques such as cyclic voltammetry (CV) or full cell studies. Herein, we present a systematic study using a welldefined model system, i.e. vertically aligned carbon nanofiber (VACNF) arrays, an interesting vertical 3D architecture with conically stacked graphitic microstructures. Density functional theory (DFT) calculations further support the electrocatalytic properties of Pt/VACNF derived from RDE measurements. We believe that this fundamental understanding would provide important insights to guide the design and characterization of future 3D architectured catalyst supports.

^zE-mail: junli@ksu.edu

In this study, we prepared VACNF arrays using a DC-biased plasma-enhanced chemical vapor deposition (PECVD) system³² and used it as a 3D architectured support for ion-beam sputtered Pt catalysts. The overall ORR catalytic activity, tolerance to methanol crossover, and recovery from CO poisoning were evaluated. It is noteworthy that many studies in literature reported similar materials such as vertically aligned CNTs⁷ or MWCNTs, ^{7,30} referred as "VACNTs." Here we use the terminology "VACNFs" following the relevant previous studies^{32–34} to stress two important differences from those VACNT materials. First, in a typical VACNF array, each nanofiber freely stands on the conductive substrate with an areal density of 1×10^9 CNFs cm⁻² (corresponding to an average interfiber distance of \sim 340 nm). Such an open structure allows Pt to be sputter-deposited from above and spread along the full length of individual nanofibers, hence enabling effective utilization of the Pt catalyst. In contrast, the VACNTs have about 4 to 10 times higher areal density, smaller diameter (20-30 nm) and larger length (30 to 1000 μ m). Thus, VACNTs are wavy and heavily entangled, giving much smaller open space that can be accessed directly from above. Second, VACNFs consist of graphitic cones stacked on top of each other along the fiber axis and present a high density of graphitic edge sites at the sidewall. 32,33,35 This is critically different from the graphite basal plane-like sidewall in CNTs or amorphous structure in common pyrolytic carbon nanofibers. These exposed graphitic edges act as the active sites and are expected to improve the durability of Pt catalysts as demonstrated with materials of similar structures.² DFT calculations based on the atomic model of conically stacked VACNF structure successfully validates the stronger binding between Pt and graphitic edges and illustrates the molecular ORR pathways. Furthermore, the 3D architectured Pt/VACNF catalyst presents interesting new phenomena in RDE studies and displays a notable resistance to methanol oxidation reaction and a higher capability to recover from CO poisoning.

Experimental

Materials.—Graphite papers (0.2 mm thick) were purchased from Toyo Tanso USA, Inc. (Troutdale, OR). The commercial Pt/ C catalyst (20 wt% Pt on Vulcan XC-72) was purchased from Alfa Aesar (Tewksbury, MA). The 5 wt% Nafion solution and methanol were purchased from Sigma-Aldrich (St. Louis, MO). Potassium hydroxide (KOH) of ACS grade was purchased from Fisher Scientific (Hampton, NH). All aqueous solutions were prepared using ultrapure water (18.2 MΩ.cm at 25 °C) from a Millipore water system (EASYPURE II, Thermo Scientific, Waltham, MA).

Preparation of Pt/VACNFs.—A graphite paper (GP) of 1 × 1 inch² was coated with a nominal thickness (equivalent to the film thickness on a flat surface) of 22 nm nickel film as the catalyst for VACNF growth using a high-resolution ion beam coater (Model 681, Gatan Inc., Pleasanton, CA). VACNFs were grown on the graphite paper using a PECVD system (Black Magic, AIXTRON, Santa Clara, CA) following the previously reported procedure. 32,33,38 Initially, the pretreatment process was performed by heating the Nicoated graphite substrate to 500 °C in 250 sccm NH3 at a pressure of 3.9 Torr for 150 s followed by a 40 W DC plasma treatment for 60 s. The combined effects of thermal dewetting and NH₃ plasma etching broke the Ni film into randomly distributed Ni NPs that catalyzed the growth of uniform VACNFs in a tip growth mode. 32,33 These Ni NPs play a major role in determining the diameter and areal density of the VACNFs. After the pretreatment, a mixture of NH₃ (250 sccm) and acetylene (63 sccm) was introduced as the precursors at 750 °C at a pressure of 4.6 Torr. The plasma power was kept at 45 W for 30, 60, and 90 min to obtain VACNFs with an average length of 5, 8, and 11 μ m, respectively. Pt of 99.99% purity was deposited on the as-grown VACNFs using the high-resolution ion beam coater under a pressure of 2×10^{-4} Torr. The sample stage was inclined at an angle of 5° and rotated at a constant speed of 15 rotations per min (rpm) to ensure uniform deposition. The deposited rate was

controlled at 0.5 Å s^{-1} . The deposition was precisely controlled to the nominal thickness of 3, 5, 10, and 20 nm, respectively, using an in-situ quartz crystal microbalance (QCM) and was further validated with scanning electron microscopy (SEM). The error of the nominal thickness is generally lower than 5%.

Characterization.—The surface morphology of the as-grown VACNF arrays was characterized by a Field-emission SEM (FESEM) (Versa 3D Dual Beam, FEI, Hillsboro, OR) at a 15-kV accelerating voltage. The microstructure of the Pt/VACNF was analyzed using field-emission scanning/transmission electron microscopy (S/TEM, FEI Tecnai F20 XT, Hillsboro, OR) at a 200-kV accelerating voltage. Elemental analysis and mapping were done using energy-dispersive X-ray spectroscopy (EDS) in the S/TEM. Raman spectra were obtained using a DXR Raman microscope (Thermo Scientific, Waltham, MA) at an excitation laser wavelength of 532 nm.

Electrode preparation.—A RDE with a glassy carbon disk of 3.15 mm diameter (0.078 cm² area) in a 12 mm diameter polyether ether ketone (PEEK) shroud was used for characterizing the catalysts. The Pt/VACNF on graphite paper was punched into 6.0 mm diameter discs and attached on the RDE using a conductive silver paste followed by drying at 70 °C before use. The Pt/VACNF electrode with 3, 5, 10, and 20 nm nominal Pt thicknesses have a Pt mass loading of 6.5, 10.8, 21.5, and 43 μ g cm⁻², respectively. For comparison, the commercial Pt/C catalyst was deposited onto the RDE as a conventional thin-film electrode from a catalyst ink. The standard ink solution consisted of 5.0 mg of the commercial Pt/C catalyst dispersed in 2.5 ml water, isopropanol and Nafion (at 200:49:1 volume ratio) mixture and was sonicated for 1 h before use. About 5.0 μ l of this ink solution was dropcast on the RDE electrode to give a Pt loading of 25.6 μ g cm⁻². After drying at the room temperature, it forms a uniform thin catalyst film. For other Pt loadings, the concentration of the Pt/C ink was adjusted proportionally.

Electrochemical measurements.—The electrochemical properties and the catalytic activity of the Pt/VACNFs were studied using a CHI 760D electrochemical workstation (CH Instruments, Austin, TX) and a rotating ring disk electrode controller (RRDE-3A, ALS Co., Ltd., Japan). For comparison, the commercial Pt/C catalyst was also examined under the same conditions. The electrochemical tests were done in a three-electrode configuration consisting of the catalyst-coated RDE as the working electrode, a coiled Pt wire as the counter electrode, and a mercury-mercuric oxide (Hg/HgO) electrode with 1.0 M NaOH filling solution as the reference electrode. The electrolyte for most studies was 0.10 M KOH solution. For direct comparison with literature, the measured electrode potential (vs Hg/HgO) in this electrolyte at 25 °C is converted to the value vs the reversible hydrogen electrode (RHE), by adding 0.907 V. Cyclic voltammetry (CV) was conducted between 0.3 V and -0.9 V (vs Hg/HgO) at a scan rate of 50 mV s^{-1} . Linear sweep voltammetry (LSV) from 0.2 V to -0.5 V (vs Hg/ HgO) at a scan rate of 10 mV s⁻¹ was carried out with the RDE at the rotation speed from 500 to 3,000 rpm. The details in converting potentials vs different reference electrodes, derivation of the limiting current density J_{lim} , the half-wave potential $E_{1/2}$ and electrochemical surface area (ECSA) are described in sections 1 to 3 and Figs. S1 and S2 in the Supporting Information (available online at stacks.iop.org/ JES/167/066523/mmedia). The accelerated stress test (AST) was carried out by performing continuous potential cycling between 0.293 V and -0.307 V (vs Hg/HgO), i.e., between 1.2 V and 0.6 V vs RHE as used in the literature, 39 at a scan rate of $100 \,\mathrm{mV \ s^{-1}}$ for 5,000 cycles. Ar or O_2 was purged into the solution depending upon the type of measurements. CV curves and ORR polarization curves were collected at various cycle intervals during the AST to record the degradation of the electrocatalysts.

Computational methods.—Spin-polarized density functional theory (DFT) calculations were performed using the Vienna Ab initio Simulation Package (VASP). The Generalized Gradient Approximation (GGA) Perdew–Burke–Ernzerhof (PBE) functional was used to account for the Kohn-Sham electron exchange-correlation interactions. The projector augmented wave (PAW) method was used to represent the ionic cores. A cut-off for the plane wave basis set expansion up to 400 eV was used for all calculations. The break condition for the self-consistent iteration was set to be 1×10^{-6} eV. Ionic relaxation was stopped when the forces on all atoms are smaller than 0.05 eV/Å. Monkhorst-Pack-based k-point meshes were employed. The relaxed lattice constants for bulk graphite obtained from this setting are a=b=2.47 Å and c=6.80 Å, and in very good agreement with reported literature values of 2.46 Å, and 6.78 Å, respectively. Moreover, Grimme's DFT-D3 method was used to account for the dispersion interactions.

DFT models.—The semi-periodic fishbone models (periodic along the carbon edge) were built by cleaving the graphite layers to represent the VACNF architecture. Given the large diameter of the VACNF (∼50 to 250 nm), the small curvature of the VACNF was neglected in this model.⁴6 The dangling bonds at the broken graphitic edges at the VACNF sidewall were passivated by OH groups, which are energetically favorable in alkaline conditions. The deposited Pt NPs were located at the graphitic edge sites. The Pt atoms interacted with the open-edge C atoms directly. Furthermore, Pt structures with different numbers of atoms, from Pt₄ to Pt₂0, were constructed. It was shown that the formation energies (per Pt atom) converged (within 0.06 eV) at Pt₁₂, which was thus selected for the modeling of ORR pathways.

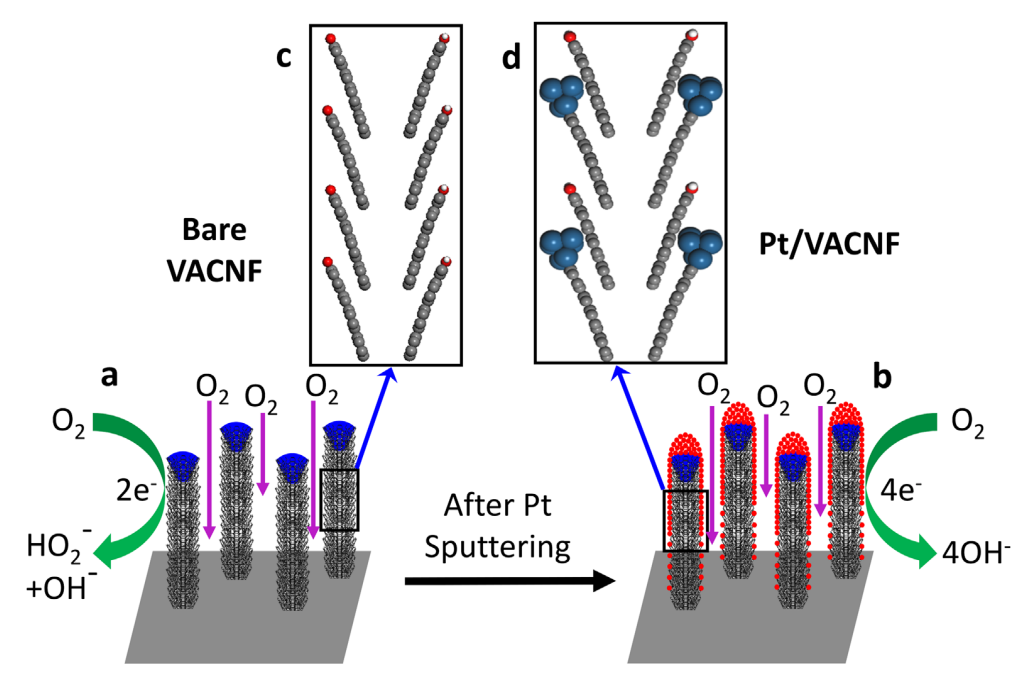
Results and Discussion

Catalyst/support design.—Scheme 1 shows the design of the ORR catalyst, where the hierarchical architecture of VACNFs is used as the catalyst support. This open vertically aligned 3D structure is significantly different from the commercial Pt/C catalysts in which the catalyst nanoparticles and carbon supports are tightly packed in a random fashion and bound through Nafion ionomer. Moreover, the microstructure of the VACNFs consists of a stack of conical graphitic cups on top of each other, providing abundant

broken graphitic edges at the sidewall. The vertical array feature and the internal graphitic stacking of the VACNFs are illustrated by FESEM and TEM images in Fig. 1. The red lines in Fig. 1c are the visual guide of the stack of a few representative graphitic sheets. The broken graphitic edges at the sidewalls are known to be the active ORR catalytic sites, ⁴⁷ which helps to anchor the Pt NPs (Figs. 1d and 1f). Panels (c) and (d) of Scheme 1 illustrate the atomic cross-sections of the proposed conically stacked VACNF architectures that are generated by cutting graphite crystal along the ($\bar{1}$ 1 10) facet.

After sputtering Pt atoms onto the VACNF arrays, it formed Pt NPs firmly attached to the exposed edge sites (as pointed by the red arrows in Fig. 1e). The large spacing (~300 nm) between the neighboring VACNFs allows the Pt NPs to spread along the fibers and reach till the bottom. The catalytic activities of the bare VACNFs and Pt/VACNFs have been studied systematically to reveal the contributions of each component. It is noteworthy that this vertically aligned architecture is free of Nafion binder, which facilitates faster mass transport of O2 via diffusion into the open structure during RDE measurements as shown in Scheme 1. In contrast, in conventional ORR catalysts, O2 molecules have to diffuse through the Nafion binder to reach Pt/C catalyst inside the film, thus requiring very thin films (<200 nm). These differences make it necessary to modify the algorithm to extract useful information from RDE experiments with the thick 3D catalyst architectures comparing to conventional thin-film catalysts. To make it clear, the methods to derive critical ORR catalytic parameters such as the limiting current density (J_{lim}) , half-wave potential $(E_{1/2})$, and electrochemical surface area (ECSA) are defined in sections 1-3 and Figs. S1 and S2 of the Supporting Information.

Structural characterization of the Pt/VACNF catalysts.—The FESEM images of the as-grown VACNFs presented in Figs. 1a and 1b show that the VACNFs are firmly attached to the surface of the graphite paper (GP) in a uniform vertical alignment and are fully separated from each other. The VACNFs are randomly distributed with the average inter-fiber spacing of \sim 340 nm (corresponding to an areal density of \sim 1 × 10⁹ CNFs cm⁻²). The diameter of VACNFs spreads from 50 nm to 250 nm with the average value of \sim 150 nm and the length ranges from 5 μ m to 11 μ m depending



Scheme 1. Schematic illustration of the catalyst structure: (a) bare VACNFs, (b) Pt/VACNFs, (c) the atomic cross-sections of the conically stacked VACNF architectures that are generated by cutting graphite crystal along the $(\bar{1} \ 1 \ 10)$ facet, and (d) Pt nanoparticles bound to the graphitic edges of the VACNFs.

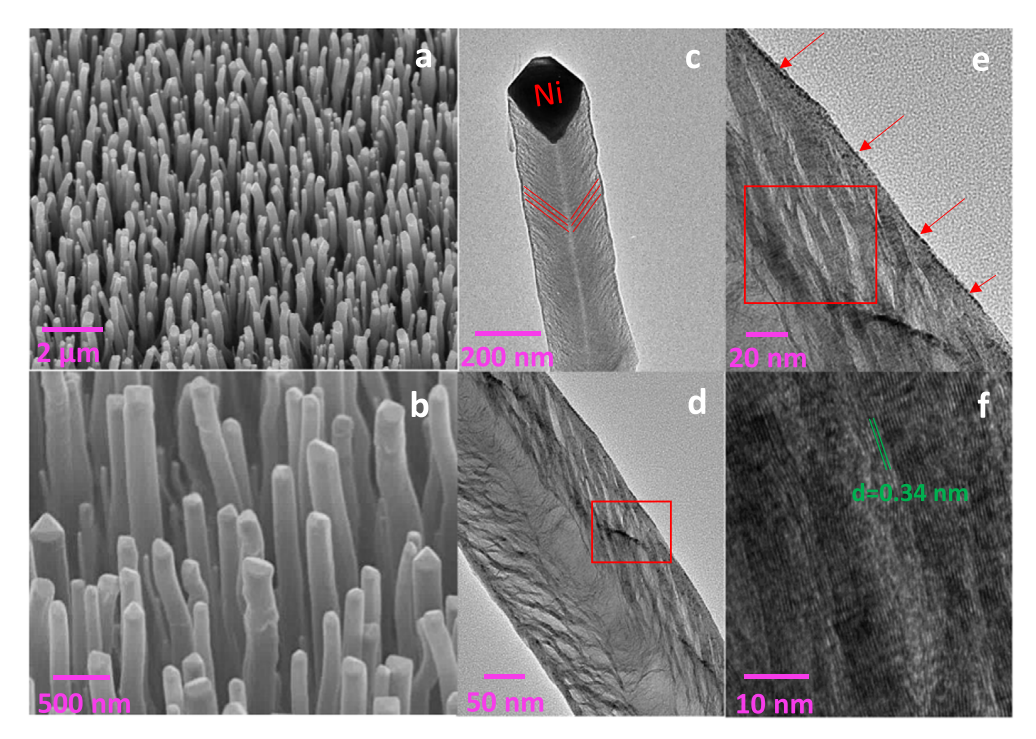


Figure 1. FESEM images of VACNF at (a) low magnification and (b) high magnification; (c) a low-magnification TEM image of a bare VACNF; TEM images of Pt/VACNF ($10.8 \mu g \text{ cm}^{-2}$) at (d) low magnification, (e) higher magnification, and (f) highest magnification showing the lattice fringe of the graphitic layers. The red boxes in panels (d) and (e) indicate the selected area for the next enlarged TEM images.

on the growth time as shown by the cross-sectional FESEM images in Fig. S3. This unique brush-like structure is different from the dense and entangled vertically aligned CNTs in other studies.^{7,30,48} In VACNF arrays, each CNF consists of a stack of conical graphitic cups under the Ni catalyst NPs as shown in Fig. 1c. The basal planes of the graphitic layers are stacked and buried inside the VACNFs leaving mainly the edge sites exposed at the sidewall. The Ni catalyst presents in the form of an "inverse teardrop" at the tip of each VACNF and acts as a cap to the bamboo-like hollow core. The Ni NPs were found to have no effects on the ORR catalysis in control experiments after removing them by soaking in 0.10 M HNO₃. The TEM image in Fig. 1d shows the tiny Pt NPs deposits on the sidewall of the VACNF array by ion-beam sputtering at a nominal thickness of 5 nm (corresponding to $10.8 \,\mu\mathrm{g}\,\mathrm{cm}^{-2}$ Pt loading relative to the geometric surface area). The enlargement of the indicated region (in red rectangle) is given in Fig. 1e, which together with the histogram in Fig. S4a indicate that the Pt NPs have an average diameter of ~ 1.1 nm. The high magnification TEM image shown in Fig. 1f displays the lattice fringes with d = 0.34 nm, which confirms the graphitic nature of the VACNFs.

Since the individual fibers are well separated, the sputtered Pt can reach deep into the 3D structure. Tilting the substrate surface normal at an angle of 5° off from the incoming Pt flux was found to give the most effective Pt deposition onto the VACNF array. Increasing the nominal thickness of the Pt deposition was found to increase the Pt nanoparticle size on the VACNF sidewall, as confirmed by the TEM images in Fig. S4. The average diameter of the Pt NPs is 1.14 ± 0.25 , 1.69 ± 0.50 , and 3.10 ± 0.43 nm for the 5, 10, and 20 nm nominal thickness (corresponding to the Pt loading of 10.8, 21.5, and $43 \mu g \text{ cm}^{-2}$), respectively. These sizes are in the right range for highly active Pt catalysts. ⁴⁹ Above 20 nm nominal Pt thickness, the deposited Pt NPs start to extend into secondary nanowhiskers anchored on the VACNFs. The high-angle annular dark-field scanning transmission electron microscope (HAADF-STEM) and the EDS elemental mapping in the selected region of a sample deposited with 5 nm nominal thickness of Pt (Fig. S5) further reveal the uniform distribution of Pt NPs on the VACNF surface. The wt%

of Pt on the Pt/VACNF can be calculated by estimating the mass of carbon present in the VACNFs and the amount of Pt deposited on the VACNFs. The mass of carbon in the VACNFs can be calculated from the average structure observed by FESEM (Figs. 1a, 1b and S3b), giving $\sim\!177~\mu\mathrm{g}~\mathrm{cm}^{-2}$ for a VACNF array with 5 $\mu\mathrm{m}$ average length and 150 nm average fiber diameter. As the Pt loading increases, the wt% of Pt on VACNF increases. The wt% of Pt on VACNFs are estimated to be $\sim\!3.5, 5.8, 10.8,$ and 19.8 wt% for the Pt loading of 6.5, 10.8, 21.5, and 43 $\mu\mathrm{g}~\mathrm{cm}^{-2}$, respectively.

It needs to emphasize that the internal microstructure of VACNFs are critically different from multi-walled carbon nanotubes (MWCNTs) in literature, ^{7,30} which is reflected by the drastically different Raman spectra in Fig. S6. The VACNF array shows a much stronger D-band peak at 1341 cm⁻¹, whose intensity is close to that of the G-band peak at 1580 cm⁻¹. The 2D band shifts up to ~2850 cm⁻¹ and becomes much broader. These evidences indicate that more sp³ carbon present in the VACNFs, most likely at the broken graphitic edges on the sidewall of VACNFs, which is consistent with the conical stacked graphitic structure revealed by the TEM images in Figs. 1c–1f. The uniform vertical alignment, much lower areal density and free of entanglement between the neighbors make it possible to deposit Pt more uniformly along the VACNFs instead of accumulating near the tips.³⁰

Assessment of the fundamental electrocatalytic properties of Pt/VACNF in ORR.—The electrocatalytic activity of the 3D architectured catalysts was first evaluated with CV in Ar-saturated and O₂-saturated 0.10 M KOH solution. Figs. 2a and 2b are representative CVs of the commercial Pt/C catalyst with a Pt loading of 25.6 μ g cm⁻² (denoted as 25.6 Pt/C) and in-house prepared Pt/VACNF catalyst with a Pt loading of 21.5 μ g cm⁻² (denoted as 21.5 Pt/VACNF), respectively. The current density is relative to the geometric area of the working electrode. In Fig. 2a, the reduction peak at -0.2 V (vs Hg/HgO) in Ar corresponds to reducing Pt oxide to Pt whereas the reduction peaks between -0.45 V and -0.75 V correspond to the hydrogen underpotential deposition (UPD) on the Pt surface. The increased reduction current observed at potentials

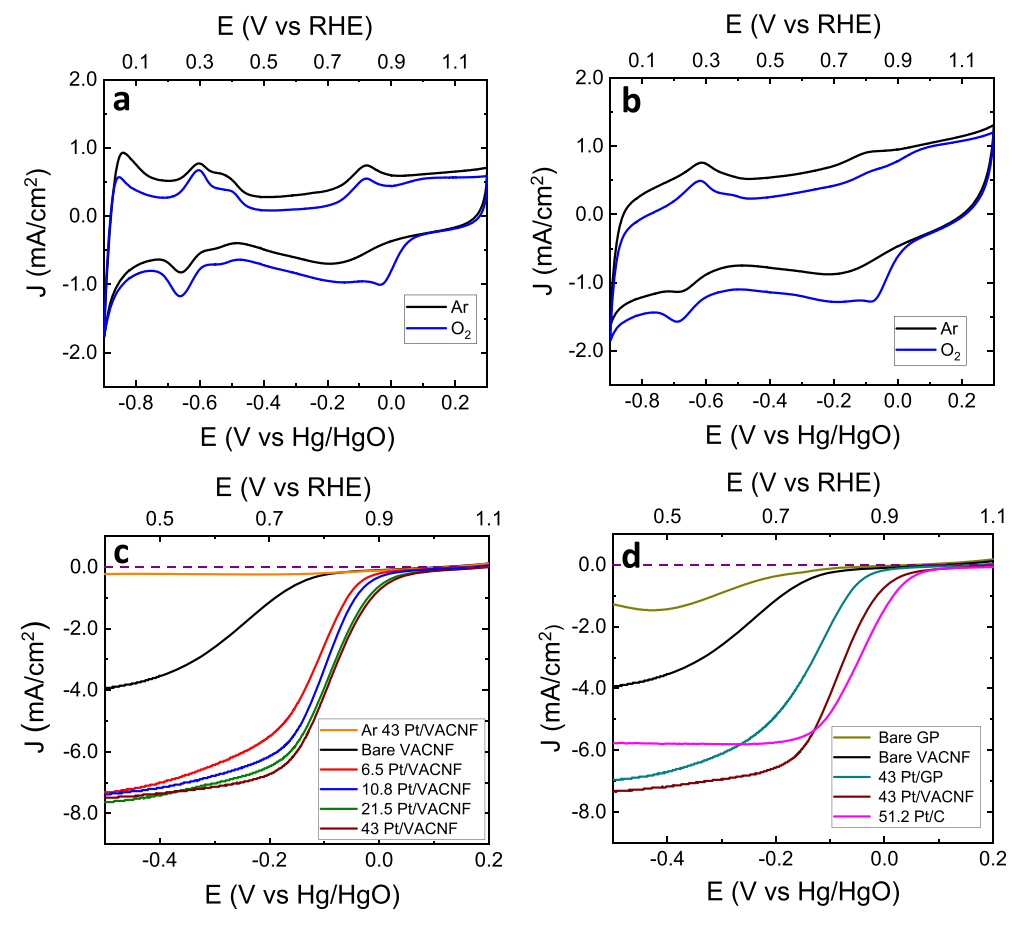


Figure 2. Cyclic Voltammetry of (a) Pt/C (25.6 μg cm⁻²) and (b) Pt/VACNF (21.5 μg cm⁻²) recorded in Ar-saturated (black line) and O_2 -saturated (blue line) 0.10 M KOH solution at a scan rate of 50 mV s⁻¹; LSV curves recorded at a scan rate of 10 mV s⁻¹ and a rotation speed of 1,600 rpm in O_2 -saturated 0.10 M KOH solution for (c) various VACNF catalysts (with a Pt loading of 0, 6.5, 10.8, 21.5 and 43 μg cm⁻²) and (d) bare graphite paper, bare VACNF, Pt on graphite paper (43 μg cm⁻²), Pt/VACNF (43 μg cm⁻²) and Pt/C (51.2 μg cm⁻²). The purple dashed lines mark the zero current density.

below 0.0 V (vs Hg/HgO) in O_2 -saturated solution is attributed to ORR. The 21.5 Pt/VACNF catalyst in Fig. 2b shows similar ORR and hydrogen adsorption features, but they are superimposed on a higher baseline current due to the larger capacitive current. The CVs for Pt/VACNF at other Pt loadings in Fig. S7 shows similar features. As the Pt loading increases, the oxygen reduction and hydrogen UPD current density increases.

The CV curves indicate that the Pt/VACNF has about 50% higher capacitance contribution compared to the Pt/C catalyst. The high capacitive contribution of Pt/VACNF catalysts arises mainly from the graphite paper that is used as the substrate to grow VACNFs. Fig. S8a presents the CV curves in Ar-saturated 0.1 M KOH for bare GP alone and those of VACNFs grown on GP with PECVD growth time of 30, 60 and 90 min. The capacitance relative to the geometric surface area of these electrodes is summarized in Figs. S8b and S8c. The bare 200 μ m thick graphite paper has a very high capacitance of $10080 \pm 105 \ \mu\text{F cm}^{-2}$, which is about 50% higher than the capacitive background of Pt/C catalyst. After the VACNFs are grown on the substrate, the capacitance is slightly higher, and it increases with the VACNF length. With 11 μ m long VACNFs (90 min growth time), the capacitance increases by \sim 11% compared to the bare graphite paper. Table SI summarizes the length and capacitance for just VACNFs after correcting the contribution from bare graphite paper. The baseline of the CV in Pt/VACNF shows a slope about two times of that of the Pt/C catalyst (see Figs. 2a and 2b), indicating a smaller ohmic resistance of the Pt/VACNF electrode due to the larger surface area and absence of Nafion coating. It is noted that the graphite paper substrate obscures some details of CVs and it gets difficult to extract the ECSA for low Pt

loadings. But for 20 nm nominal thickness of Pt (43 μ g cm⁻²) on the VACNFs, the ECSA was estimated to be 23.5 m² g⁻¹ as shown in Fig. S2. This is lower than the 28.6 m² g⁻¹ obtained with commercial Pt/C, which is mainly due to the larger Pt NPs on the VACNF tip surface which approximately accounts for about ~20% of the deposited Pt in proportion to its geometric surface area. More uniform Pt distribution and higher ECSA can be achieved in the future using other deposition techniques like atomic layer deposition (ALD).

The linear sweep voltammetry (LSV) curves of the bare VACNF and Pt/VACNF catalysts (at 6.5, 10.8, 21.5, and 43 μg cm⁻² Pt loading) recorded with the RDE from +0.20 V to -0.50 V (vs Hg/ HgO) at a rotating speed of 1,600 rpm in O₂-saturated 0.10 M KOH is shown in Fig. 2c. All LSVs in the O₂-saturated solution present the characteristic sigmoidal curves indicating the formation of the steady-state. However, compared to the commercial Pt/C catalyst, the baseline in the diffusion-controlled region is slanted downward to the negative potential. Nevertheless, the limiting current density J_{lim} and the half-wave potential $E_{1/2}$ can be derived from each LSV curve by extrapolating the linear segments as described in Fig. S1 of the Supplementary Information. Table I summarizes the J_{lim} (background-corrected) and $E_{1/2}$ (vs both Hg/HgO and RHE) for different catalysts. Quantitatively, the capacitive current arising from the VACNF structure and the GP in Pt/VACNF is similar in both CV and LSV measurements and can be calculated from the total capacitance derived from Fig. S8a. It was found to be only about -0.1 mA cm^{-2} in the LSV curve in Fig. 2c, which is negligible compared to the measured ORR limiting current density (~6 mA cm⁻²). The LSV of 43 Pt/VACNF recorded in the absence of O₂ (in

Table I. Summary of the limiting current density J_{lim} (background-corrected) and half-wave potential $E_{1/2}$ for different catalysts. The LSVs in Arsaturated electrolyte is subtracted from the ORR LSVs measured in O_2 -saturated electrolyte before quantitative analyses.

Catalyst	J_{lim} (mA/cm ²)	$E_{1/2}$ (V vs Hg/HgO)	$E_{1/2}$ (V vs RHE)
Bare GP	1.2	-0.291	0.616
Bare VACNF	3.5	-0.247	0.660
6.5 Pt/VACNF	6.3	-0.118	0.789
10.8 Pt/VACNF	6.5	-0.102	0.805
21.5 Pt/VACNF	6.6	-0.091	0.816
43 Pt/VACNF	6.7	-0.086	0.821
43 Pt/GP	5.8	-0.131	0.776
51.2 Pt/C	5.7	-0.045	0.862

Ar-saturated solution) shows only a small maximum current density of $-0.2 \,\mathrm{mA\,cm^{-2}}$ at $-0.50 \,\mathrm{V}$ (vs Hg/HgO) (indicated by the orange solid line), which accounts for the total contribution from surface redox reactions, ohmic current, and capacitive current. This is subtracted from the ORR LSVs in data analyses. It is clear that the LSV curves of Pt/VACNF samples slightly vary with the Pt loadings at low values but almost superimpose on each other when the Pt loading is above $21.5 \,\mu\mathrm{g\,cm^{-2}}$. Interestingly, the bare VACNF/graphite paper alone also shows a sigmoidal curve, but the much lower J_{lim} and $> 120 \,\mathrm{mV}$ negative shift of $E_{1/2}$ than the Pt/VACNF catalysts indicates that the bare VACNF arrays act as an inefficient ORR catalyst, possibly through the 2-e⁻ reduction pathway.

It is noteworthy that the J_{lim} values (6.3–6.7 mA cm⁻²) of all the Pt/VACNF catalysts are higher than the value of ~5.7 mA cm⁻² determined by the Levich equation at 1,600 rpm for the benchmark system, i.e. the conventional ultrathin Pt/C catalyst films. To reveal the reasons, systematic LSV experiments were performed with the bare graphite paper (GP), bare VACNFs grown on GP, and VACNFs on GP sputter-coated with 43 μ g cm⁻² Pt. The LSV data in RDE experiments are systematically compared with the commercial Pt/C thin film catalyst at 51.2 μ g cm⁻² Pt loading. As shown in Fig. 2d, the 51.2 μ g cm⁻² Pt/C catalyst shows an ORR J_{lim} = 5.7 mA cm⁻² which matches the theoretical value and exhibits an expected $E_{1/2}$ = -0.045 V vs Hg/HgO (i.e. 0.862 V vs reversible hydrogen electrode (RHE)). These benchmark characteristics validate that the experimental conditions are appropriate.

Interestingly, even the bare GP shows a low ORR activity ($J_{lim} =$ 1.2 mA cm⁻²) at lower potentials with $E_{1/2} = -0.291$ V vs Hg/HgO (0.616 V vs RHE). After the growth of VACNF arrays on the GP, the ORR current substantially increases to $J_{lim} = 3.5 \text{ mA cm}^{-2}$ and the LSV curve positively shifts to $E_{1/2} = -0.247$ V vs Hg/HgO (0.660 V vs RHE). After sputtering 43 μ g cm⁻² Pt onto the VACNF array, the ORR J_{lim} value jumps up to \sim 6.7 mA cm⁻², exceeding the theoretical value for thin-film Pt/C catalysts by \sim 18%. In the meantime, the LSV curve significantly shifts to higher potentials with $E_{1/2} = -0.086$ V vs Hg/HgO (0.821 V vs RHE). The $E_{1/2}$ value of Pt/VACNF with 43 μ g cm⁻² Pt loading is only 41 mV lower than the commercial Pt/C catalyst with 51.2 μ g cm⁻² Pt loading. For comparison, the bare GP (without VACNFs) sputtered with 43 μg cm⁻² Pt gives much more negative $E_{1/2} = -0.131$ V vs Hg/HgO (0.776 V vs RHE). It is noteworthy that the current density at E < -0.2 V is much higher than the theoretical limiting current density (\sim 5.7 mA cm⁻² at 1,600 rpm) by the Levich equation and is slanted. Using the linear extrapolating method in Fig. S1, the J_{lim} value is determined to be 5.8 mA cm⁻² matching well with the theoretical value. The more positive $E_{1/2}$ value of Pt/VACNF in comparison with Pt/GP confirms that the VACNFs are able to support the majority of the Pt NPs, leading to the ORR activity comparable to the well-dispersed commercial Pt/C system. However, it is surprising that both Pt/GP and Pt/VACNF (grown on GP) give high J_{lim} values exceeding the diffusion limited theoretical value obtained for Pt/C thin films. Understanding the fundamental principles behind this phenomenon is critical for design and electrochemical studies of

future 3D catalyst supports. So far, little efforts have been made to reveal the unique RDE features of the 3D catalyst films.

ORR catalysts are normally studied by drop-casting a uniform thin film (<200 nm) of the catalyst material onto the inlaid RDE. The vertically aligned 3D catalyst support is much thicker (5-11 μ m) and poses a highly porous open structure. Thus, it is substantially different from the conventional Pt/C system. Also, as shown in Fig. S9a, it is necessary to mount the VACNF arrays along with the GP substrate onto the RDE to retain the intact vertically aligned structure. Similar methods have been reported in other studies using polymer transferring films, ^{7,48,50} but the processes were not easy to control and it was hard to quantify the RDE voltammetry data. Alternatively, some studies use recessed RDEs for the non-conventional porous materials.31,51 However, this approach also has its limitations such as larger ohmic resistance and altered hydrodynamics due to the large recessing depth (typically $> 500 \mu m$). Hence it is necessary to explore RDE studies using the raised VACNF array electrodes as illustrated in Fig. S9a.

Here we systematically link the observed RDE voltammetry results with all the possible structural factors illustrated in Fig. S9a. First, the silver paste used for mounting the VACNF/GP disk onto RDE was found to have a negligible contribution towards the ORR. There is no measurable difference in LSV curves between the bare glassy carbon RDE and that applied with the Ag paste. Second, the bare GP substrate did increase the baseline current. A peak current of \sim 1.2 mA cm⁻² is observed with the bare GP disk in Fig. 2d, which increases with the rotation rate. This low ORR is at rather negative potentials. Third, after growing VACNFs on the GP disks, LSV shows a tilt sigmoidal curve with substantially higher ORR current at slightly higher potentials than the bare GP disk. Fourth, Pt/VACNF samples show LSVs approaching that of the commercial Pt/C catalyst but with a higher J_{lim} than the theoretical value by Levich equation. The control experiment using 43 μ g cm⁻² Pt directly deposited on a GP also shows higher J_{lim} than the theoretical value but with a negative shift in $E_{1/2}$ than Pt/VACNF (Fig. S9b).

As shown in Fig. S9a, when the GP disks are mounted on the RDE, the electrode surface is raised above the surrounding PEEK insulator by about 200 μ m due to the GP thickness. This is considerably larger than the thickness of the catalyst film (\sim 0.2 μ m)⁵² in traditional thin-film RDE experiments. Therefore, the resulted hydrodynamic conditions need to be re-examined. The raised GP edge is expected to give a Reynolds number larger than the critical Reynolds number⁵³ and thus will induce turbulent flow at the GP disk edge. Accordingly, the mass transfer of O₂ is larger than the ideal linear diffusion described by the Levich equation. This effect becomes more evident at higher rotation rates, as revealed by the larger tilt of the LSV curves in Fig. S9b.

The fundamental hydrodynamics of a thin-film RDE can be further illustrated with two parameters, namely the hydrodynamic boundary layer thickness y_h and the steady-state diffusion layer thickness δ_o , which are given as following ⁵³:

$$y_h = 3.6(\nu/\omega)^{1/2}$$
 [1]

$$\delta_o = 1.61 D_o^{1/3} \omega^{-1/2} \nu^{-1/6}$$
 [2]

where ω is the angular frequency in s⁻¹ and D_o is the diffusion coefficient in cm²/s. The values of these two parameters are plotted vs the rotation rate in Fig. S9c. The hydrodynamic boundary layer thickness y_h indicates the thickness of the solution rotating with the RDE. In 0.10 M KOH ($\nu = 0.01 \text{ cm}^2 \text{ s}^{-1}$) at $\omega = 1600 \text{ rpm}$ or 167.5 s^{-1} , y_h is roughly 278 μ m using Eq. 1. In this study, the 200 μ m thick GP substrate is close to y_h. Therefore, the deviation from the Levich equation is expected. This explains the slanted LSVs in the diffusion-controlled regime, which can be partially corrected by the linear extrapolating method illustrated in Fig. S1.

The second parameter δ_0 describes the steady-state diffusion layer thickness of a thin-film RDE in the diffusion-controlled regime in RDE LSVs. Based on Eq. 2, δ_0 is 1.55 μ m at 1600 rpm, which is considerably larger than the conventional 200 nm catalyst film thickness. In contrast, the average thickness of the VACNF arrays at different growth times in this study is 5, 8 and 11 μ m, respectively, much larger than δ_0 . Hence the open 3D structure of VACNF poses a secondary effect causing the LSVs in RDE experiments to deviate from the Levich model. Fig. S9b indeed shows that Pt/VACNFs on GP exhibit slightly higher J_{lim} than the Pt/GP catalyst and the difference increases with the rotation rate. Interestingly, the LSVs of the bare VACNF/GP samples (Fig. S9d) only show slight changes vs the VACNF length, clearly not in a proportional relationship. It is likely that the diffusion layer is mainly disturbed by the roughness at the outer surface ($\sim 0.5-1.0 \mu m$) rather than the full 3D brush-like VACNF structures.

Overall, the obtained high limiting current density and the tilt LSV curves of the Pt/VACNF catalysts can be rationalized with the deviation from the Levich equation by the turbulent flow at the raised GP substrate edge and the disturbance to the stagnant diffusion layer by the surface roughness of the VACNF arrays. The linear extrapolating method (see Fig. S1) can partially correct the tilt of LSVs. Thus, the general principles of RDE measurements are still applicable to such complicated 3D systems. We just need to be cautious in quantitative interpretation of the enhanced limiting current density comparing to the thin-film Pt/C catalysts. In the Pt/VACNF system, even though the ORR catalytic activity is primarily attributed to Pt NPs, the VACNF array not only provides the 3D open architecture to support Pt catalyst but also presents the synergistic ORR catalytic activity at more negative potentials.

Analyses of the rotating disk electrode measurements.—The RDE polarization curves (after background correction) at a series of rotation speed from 500 to 3,000 rpm for the commercial Pt/C catalyst at 25.6 μg cm⁻² Pt loading and the Pt/VACNF catalyst at 21.5 μg cm⁻² Pt loading are displayed in Figs. 3a and 3b, respectively. The J_{lim} for ORR increases with the rotation speed while the steady-state diffusion layer thickness δ_o is reduced. The RDE polarization curves (after background correction) for the Pt/C and Pt/VACNF catalysts (with Pt loadings of 6.5, 10.8 and 43 μg cm⁻²) are displayed in Fig. S10. Clearly, all Pt/VACNF catalysts show consistent higher J_{lim} values than the benchmark Pt/C catalyst, but the tilt of the curve in the diffusion-controlled region becomes smaller as the Pt loading increases.

The Koutecky-Levich (KL) equation has been commonly used to evaluate the kinetic parameters of the ORR reaction with conventional catalysts and is adopted for the Pt/VACNF system here. Fig. S11 shows the KL plots (i.e. 1/j vs $1/\omega^{1/2}$) for various catalysts derived at different potentials based on Eq. 3:

$$\frac{1}{I} = \frac{1}{I_b} + \frac{1}{R^{1/2}}$$
 [3]

where J is the measured current density (mA/cm²), J_k is the kinetic limited current density (mA/cm²) and ω is the electrode rotation speed (rpm). The KL plots within the potential range from -0.2 V to -0.5 V (vs Hg/HgO) presented in Fig. S11 exhibits linear lines nearly parallel to each other for each catalyst, confirming the reaction is diffusion-controlled. From the slope (1/B) of the KL plots, the overall electron transfer number (n) can be calculated using the Levich equation:

$$B = 0.20 \, nF[O_2] D_{O_2}^{2/3} \nu^{-1/6}$$
 [4]

where n is the electron transfer number in ORR, F is the Faraday constant (96,485 C mol⁻¹), $[O_2] = 1.2 \times 10^{-6}$ mol cm⁻³ is the dissolved O₂ concentration in 0.10 M KOH, $D_{O_2} = 1.90 \times 10^{-5} \text{ cm}^2$ s⁻¹ is the diffusion coefficient of O_2 in 0.10 M KOH and $\nu=0.01$ cm² s⁻¹ is the kinematic viscosity of 0.10 M KOH solution. Fig. 3c shows the KL plot derived using the J_{lim} at $-0.4~{\rm V}$ (vs Hg/HgO) for 25.6 Pt/C and J_{lim} derived from the linear extrapolation method (see Fig. S1) for bare VACNF, 21.5 Pt/GP and 21.5 Pt/VACNF. The derived n values are 2.9, 3.9, 4.7 and 5.1, respectively. The 25.6 μ g cm⁻² Pt/C catalyst gives n = 3.9, close to the benchmark value of 4.0 for the direct reduction of O₂ through the 4-e⁻ pathway. This validates the experimental conditions and the algorithm of the KL analyses. However, the as-derived value n = 2.9 for the bare VACNF array is greater than n = 2 for the 2-e⁻ ORR pathway while n = 4.7 for 21.5 Pt/GP and n = 5.1 for Pt/VACNF are greater than n = 4 for the 4-e⁻ pathway. As discussed above, this is associated with the enhanced J_{lim} by the thick GP substrate, which causes the LSV to deviate from the Levich equation. Modification to the Levich equation is needed to apply the KL analyses on 3D catalyst structures. The contribution of the 3D morphology⁵⁴ and their effects on KL analyses of carbon-based electrocatalysts⁵⁵ have indeed received attention recently. While more accurate algorithms need to be developed in the future, here we hypothesize that the Pt catalysts on the 3D VACNF support follow the direct 4-e transfer ORR pathway similar to traditional Pt/C catalysts.

DFT simulation of the ORR mechanism of the VACNF catalyst support.—The dissociative and associative 4-e $^-$ ORR mechanisms on Pt (111) in alkaline solutions are adopted in this study. $^{56-59}$ As shown by Eqs. 5–8, the dissociative ORR pathway follows a direct O–O bond cleavage of O_2^* . For each dissociated O*, one H is abstracted from liquid H₂O(l), coupled with the charge transfer of one electron to form OH $^-$ ion and OH* (Eq. 8). The combination of OH* coupled with a second charge forms a second OH $^-$ ion.

$$O_2(g) + * \rightarrow O_2^*$$
 [5]

$$O_2^* + * \rightarrow 2O^*$$
 [6]

$$O^* + H_2O(l) + e^- \rightarrow OH^* + OH^-(aq)$$
 [7]

$$OH^* + e^- \to ^* + OH^-(aq)$$
 [8]

In the associative mechanism shown in Eqs. 9–10), O_2^* first abstracts one H atom from H_2O (l) producing OOH* and an OH⁻ ion (first charge transfer), followed by the O–O bond cleavage to produce OH* and O*. Both O* and OH* proceed to form OH⁻ by following steps as in Eqs. 7–8.

$$O_2^* + H_2O(l) + e^- \rightarrow OOH^* + OH^-(aq)$$
 [9]

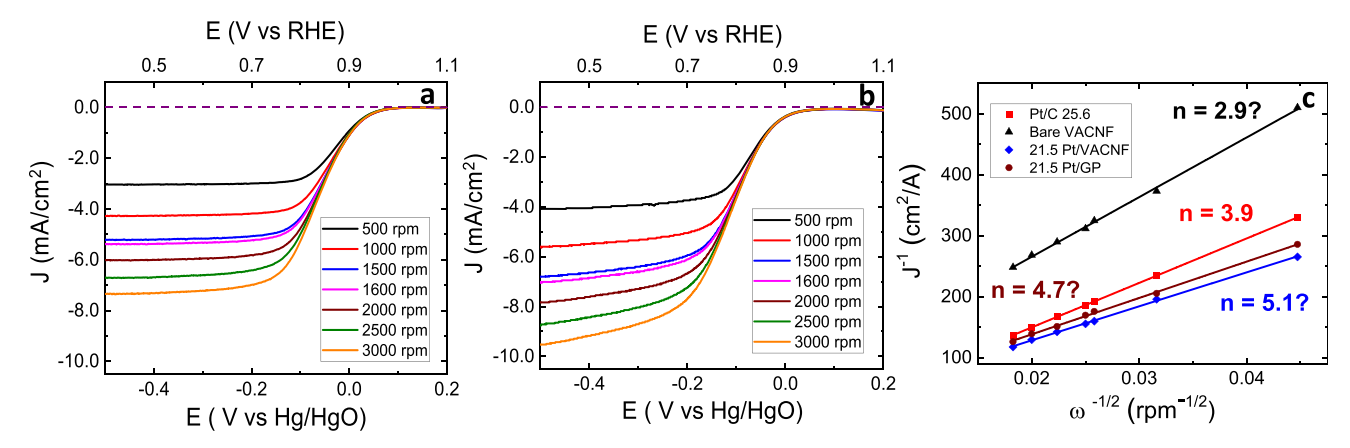


Figure 3. Rotating disk electrode voltammogram with background-corrected for (a) Pt/C (25.6 μ g cm⁻²) and (b) Pt/VACNF (21.5 μ g cm⁻²) recorded in 0.10 M KOH solution with a scan rate of 10 mV s⁻¹ at a series of rotation speed from 500 to 3,000 rpm. The purple dashed line marks the zero current density; (c) KL plot derived using background-corrected J_{lim} at -0.4 V (vs Hg/HgO) for Pt/C (25.6 μ g cm⁻²) and J_{lim} calculated as described in supplementary information for Bare VACNF, Pt/GP (21.5 μ g cm⁻²) and Pt/VACNF (21.5 μ g cm⁻²).

$$OOH^* + * \rightarrow OH^* + O^*$$
 [10]

Over the Pt-free VACNF, both 2-e^- and 4-e^- pathways were also considered. According to Choi *et al.*, ⁶⁰ it has been shown that O_2 adsorption is not crucial because the charge transfer initiating ORR may occur in the outer Helmholtz plane. Thus, the process involving OOH* formation can be summarized by Eq. 11. In the 2-e^- pathway, OOH* will desorb upon receiving the second electron, as in Eq. 12. In the 4-e^- pathway, OOH $^-$ further undergoes the O–O bond cleavage to form OH* and O*. At the OH-passivated VACNF edge, the formation of O* is likely to result in H₂O formation from the passivating OH groups, as described by Eqs. 13–14), where OH_{edge} and O_{edge} denote the passivating OH and O species at the graphitic edge.

$$O_2(g) + * + H_2O(l) + e^- \rightarrow OOH^* + OH^-$$
 [11]

$$OOH^* + e^- \rightarrow * + OOH^-(aq)$$
 [12]

$$OOH^* + 3OH_{edge} \rightarrow 3O_{edge} + 2H_2O(aq)$$
 [13]

$$O_{edge} + H_2 O(l) + e^- \rightarrow * + OH^-(aq)$$
 [14]

Analogous to the Computational Hydrogen Electrode (CHE) model under acidic condition,⁵⁷ the elementary charge transfer step in an alkaline environment is represented by Eq. 15. In the same way, the step involving OOH⁻(aq) is represented by Eq. 16.

$$OH^{-}(aq) + \frac{1}{2}H_{2}(g) \to H_{2}O(l) + e^{-}$$
 [15]

$$OOH^{-}(aq) + \frac{1}{2}H_{2}(g) \rightarrow H_{2}O(l) + \frac{1}{2}O_{2}(g) + e^{-}$$
 [16]

Both zero-point energy (ZPE) corrections and entropic contributions were estimated based on the simple harmonic approximation. For liquid phase water, $H_2O(l)$, the solvation energies (the free energy difference between their gas-phase and aqueous-phase states) were taken from the handbook by Dean. 62

As shown in Fig. S12, the dangling bonds at the graphitic edges are passivated with OH groups. Free energy diagrams corresponding to the 2-e⁻ and 4-e⁻ ORR pathways over bare VACNFs, along with the configurations of reaction intermediates, are presented in Fig. 4. As indicated in Fig. 4, the formation of OOH* from O₂ (g) via the first charge transfer in Eq. 9, is an exothermic process. For the 4-e⁻ process (blue line in Fig. 4), O* destabilizes the passivating OH and

converts it into oxygen atoms according to Eq. 13. This step is highly exothermic (-5.19 eV corresponding to the formations of 3 edge sites without the passivating H, as indicated by the inset figure in Fig. 4). However, the regeneration of passivating OH groups in Eq. 14 will be a highly endothermic step (1.16 eV). Thus, the 2-e^- process, simply involving the desorption of OOH* (as OOH⁻ indicated by red lines in Fig. 4) is more competitive and is consistent with the experimental results in this work.

DFT calculations based on the Pt/VACNF model confirmed that Pt atoms preferentially bind at the edge. The sputtered Pt atoms form strong Pt–C bonds with the C atoms at the graphitic edge, which stabilizes the ORR active sites. As shown in Fig. S13, the strong Pt–C interaction enables Pt to easily replace the original O species passivating the graphitic edge. Other evidence from modeling has been reported by Cheng and coworkers. ^{63,64} More detailed structures of Pt catalysts supported on VACNF models are shown in Figs. S12–S14. Upon optimization, the Pt structure becomes somewhat corrugated and also compressed due to the mismatch between Pt and graphene lattices, i.e. 2.51 Å in graphene vs 2.81 Å nearest neighbor Pt-Pt distance in Pt (111) surface.

Here, these Pt atoms are also considered to be the primary site for ORR. The molecular configurations of the most stable intermediates associated with the proposed mechanism for Pt/VACNF are shown in Fig. 5a. All ORR intermediates prefer to bind at the Pt site. The free energy diagram (Fig. 5b) shows that O₂ adsorption over Pt/ VACNF becomes much stronger (-1.45 eV) than on Pt (111)(-0.60 eV). Thus, the overall ORR free energy profile for the Pt/ VACNF system shifts notably downward. The O-O bond cleavage is also an exothermic step (-1.19 eV). Subsequent formation of OH* (a one-electron transfer step, Eq. 7) and its desorption to form $OH^{-}(aq)$ (Eq. 8) are both exothermic at -1.12 eV and -0.05 eV, respectively. In comparison, over Pt/VACNF, the associative mechanism proceeds through the formation of OOH* in Eq. 9, with a free energy change of -0.01 eV. As shown in Fig. 5, the formation of atomic O species via the dissociative mechanism would be much more thermodynamically favorable. Interestingly, by applying a potential bias of 1.23 V, the free energy diagram (Fig. S15) suggests that the OH desorption step becomes strongly endothermic (1.18 eV) and likely the rate-limiting step. Furthermore, the limiting potential calculated on Pt/VACNF is 0.05 V, which is lower than 0.45 V on Pt (111), due to the strong OH binding at the low coordinated Pt sites in our Pt/VACNF model (see Fig. 5). The DFT calculations are consistent with the -41 mV shift in $E_{1/2}$ with Pt/VACNF comparing to the Pt/C (see Fig. 2d).

Evaluation of the durability of Pt/VACNF electrocatalysts.— After rationalizing the RDE LSVs, we can now adapt RDE for

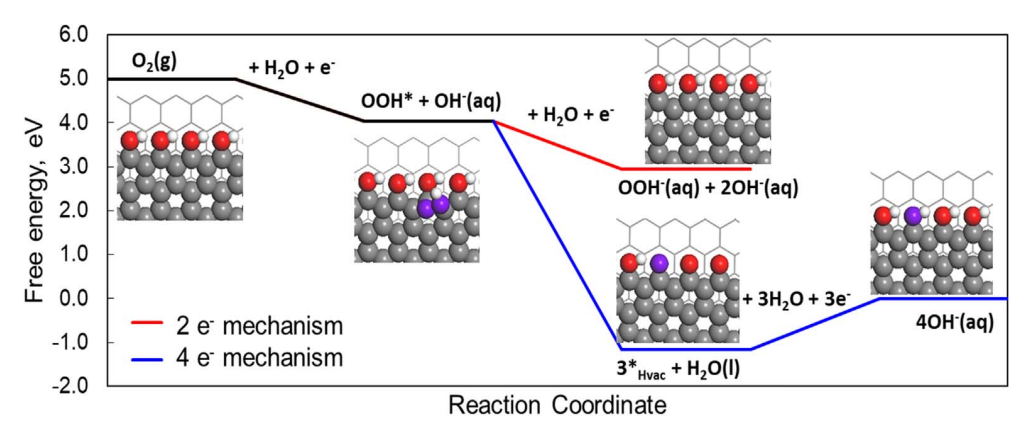


Figure 4. Free energy diagram comparing the 2-e⁻ associative pathway (red) with 4-e⁻ pathway (blue) on as-grown VACNFs. Color code: white—H, red—O, gray—C, purple—O from the reactant.

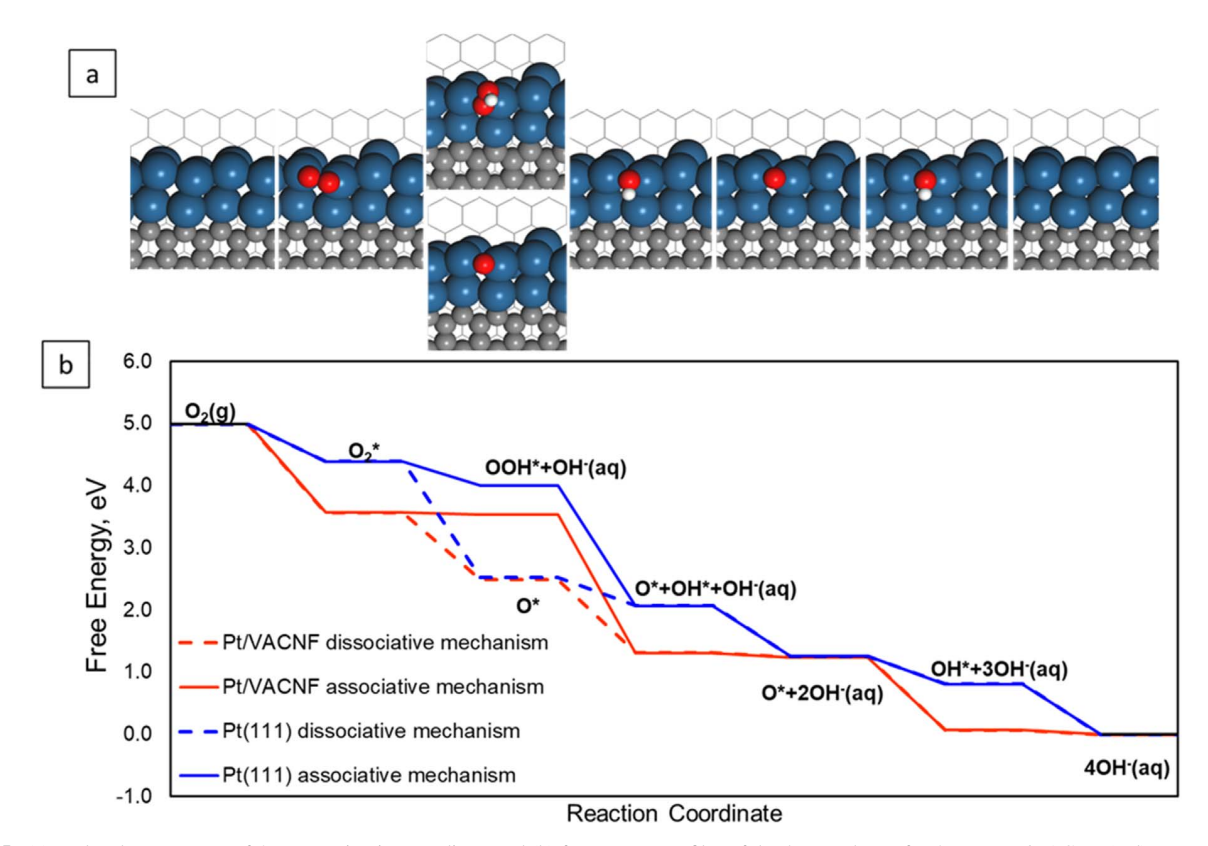


Figure 5. (a) Molecular structures of ORR reaction intermediates and (b) free energy profiles of the 4-e⁻ pathway for ORR on Pt/VACNF (red) comparing with Pt (111) (blue) by both dissociative (dashed lines) and associative mechanisms (solid lines). Color code: white—H, red—O, gray—C, blue—Pt.

further studies. One of the objectives is to understand whether Pt/VACNF catalysts show better durability due to the strong binding of Pt NPs on the graphic edge sites as revealed by the DFT calculations. To evaluate the durability of the synthesized Pt/VACNF catalysts in comparison with the commercial Pt/C catalysts, low Pt loading (10–13 μ g cm $^{-2}$) has been studied with the accelerated stress test (AST) in O₂-saturated 0.10 M KOH between 0.293 V and -0.307 V vs Hg/HgO (i.e. 1.2 V and 0.6 V vs RHE) at a scan rate of 100 mV/s. After every 1,000 cycles of AST, LSV (at 1,600 rpm) is recorded with RDE (Figs. S16a and S16b). Two parameters, the shift of the potential (Δ E) to maintain the original half-wave current and the % loss in the limiting current density J_{lim} , are derived and shown in Figs. S16c and S16d. As presented in Figs. S16a and S16b, the Pt/VACNF catalyst with 10.8 μ g cm $^{-2}$ Pt loading shows much more stable LSV curves than the commercial Pt/C catalyst with a slightly higher Pt loading of 12.8 μ g cm $^{-2}$. The potential shift Δ E after

5,000 AST cycles is about -140.0 mV with the Pt/VACNF whereas it is -250 mV for the commercial Pt/C catalyst. The percentage loss of J_{lim} in the Pt/VACNF catalyst is only $\sim 18\%$ after 5,000 AST cycles in contrast to 50% in Pt/C catalysts. The average sizes of the Pt nanoparticles in Pt/VACNF catalyst and Pt/C catalyst are about 1.1 nm and 3.5 nm, respectively. Even the smaller Pt NPs on the VACNF exhibit better durability than the Pt/C catalyst. This could be likely attributed to the strong interactions between Pt NPs and the graphitic edges. The durability can be further improved by increasing the Pt loading as shown in Fig. S17, and it is clear that 43 μ g cm $^{-2}$ Pt/VACNF is still better than 51.2 μ g cm $^{-2}$ Pt/C. The TEM images before and after 5,000 AST cycles in Fig. S18 further shows the severe dissolution and agglomeration of Pt in Pt/C whereas much smaller changes were observed in Pt/VACNFs.

Tolerance to methanol crossover reaction.—For DMFCs, the ideal ORR catalyst should exhibit higher tolerance to methanol crossover from the anode. These have been investigated by a sideby-side comparison of the Pt/VACNF catalyst (at 10.8 and $21.5 \,\mu \mathrm{g \, cm^{-2}}$ Pt loadings) with the commercial Pt/C catalyst (at 12.8 and 25.6 μ g cm⁻² Pt loadings). The methanol tolerance was evaluated by performing amperometric measurements and record j-t curves while adding 3.0 M methanol into 0.10 M KOH in 20 steps at 0.2 ml/step followed by 8 steps at 2.0 ml/step. The final methanol concentration was 0.75 M in the electrolyte solution. Two fixed potentials, $-0.30\ V$ and $-0.10\ V$ (vs Hg/HgO) were chosen for the amperometric measurements, corresponding to the diffusion-controlled and mixed kinetic-diffusion controlled ORR regions of the LSV curves in Fig. 2c. As shown in Fig. 6a, at -0.30 V, the commercial Pt/C is very sensitive to methanol, with the current density dropping from about -5.0 mA cm^{-2} to -2.0 mA cm^{-2} after adding methanol. In contrast, the current density of Pt/VACNF only drops from -6.5 mA cm^{-2} to -4.4 mA cm^{-2} , retaining 67% of the original ORR current. At -0.1 V (Fig. 6b), where there is stronger methanol oxidation, the difference between the commercial Pt/C and the Pt/VACNF is even more evident. For the commercial Pt/C, the current density changes from -4.4 mA cm^{-2} (dominated by ORR) to $+3.6 \text{ mA cm}^{-2}$ (dominated by methanol oxidation). In contrast, with the Pt/VACNF, the current density is dominated by ORR even after reaching the final methanol concentration of 0.75 M though the

magnitude is reduced by \sim 50%, from -3.4 mA cm^{-2} to -1.7 mA cm^{-2} . This demonstrates that the VACNF support can significantly improve the tolerance to methanol crossover.

Fig. 6c presents the LSV curves at 1600 rpm for the two types of catalysts in the presence and absence of 0.75 M methanol. For the Pt/ C catalyst with 25.6 μ g cm⁻² Pt loading, the LSV curve in presence of methanol is dominated by methanol oxidation at the potential above -0.23 V (vs Hg/HgO). In contrast, the Pt/VACNF catalyst with 21.5 μ g cm⁻² Pt loading exhibits a reduction current in the full ORR potential range (up to 0.0 V vs Hg/HgO) and the methanol oxidation is significantly suppressed even up to 0.0 V (vs Hg/HgO), which explains why a large ORR current density can be observed at -0.1 V even after reaching 0.75 M methanol concentration (as shown in Fig. 6b). Figs. S19 and S20 show similar results for Pt/ VACNF catalysts with 10.8 and 43 μg cm⁻² Pt loading, respectively. The methanol oxidation is suppressed in both amperometric jt and LSV curves compared to the Pt/C catalysts at similar Pt loadings. Not surprisingly, as the Pt loading increases, the methanol crossover reactions become more dominant in the Pt/C catalyst. The observed high tolerance to methanol oxidation could be related to the stronger O₂ binding on Pt/VACNF than on Pt (111) as revealed by the DFT calculations in Fig. 5. The presence of O species on the VACNF-supported Pt NPs hinders the methanol chemisorption in the mixed environment of O₂ and methanol. Overall, the adsorption of methanol on active Pt sites in Pt/VACNF is weaker than that of

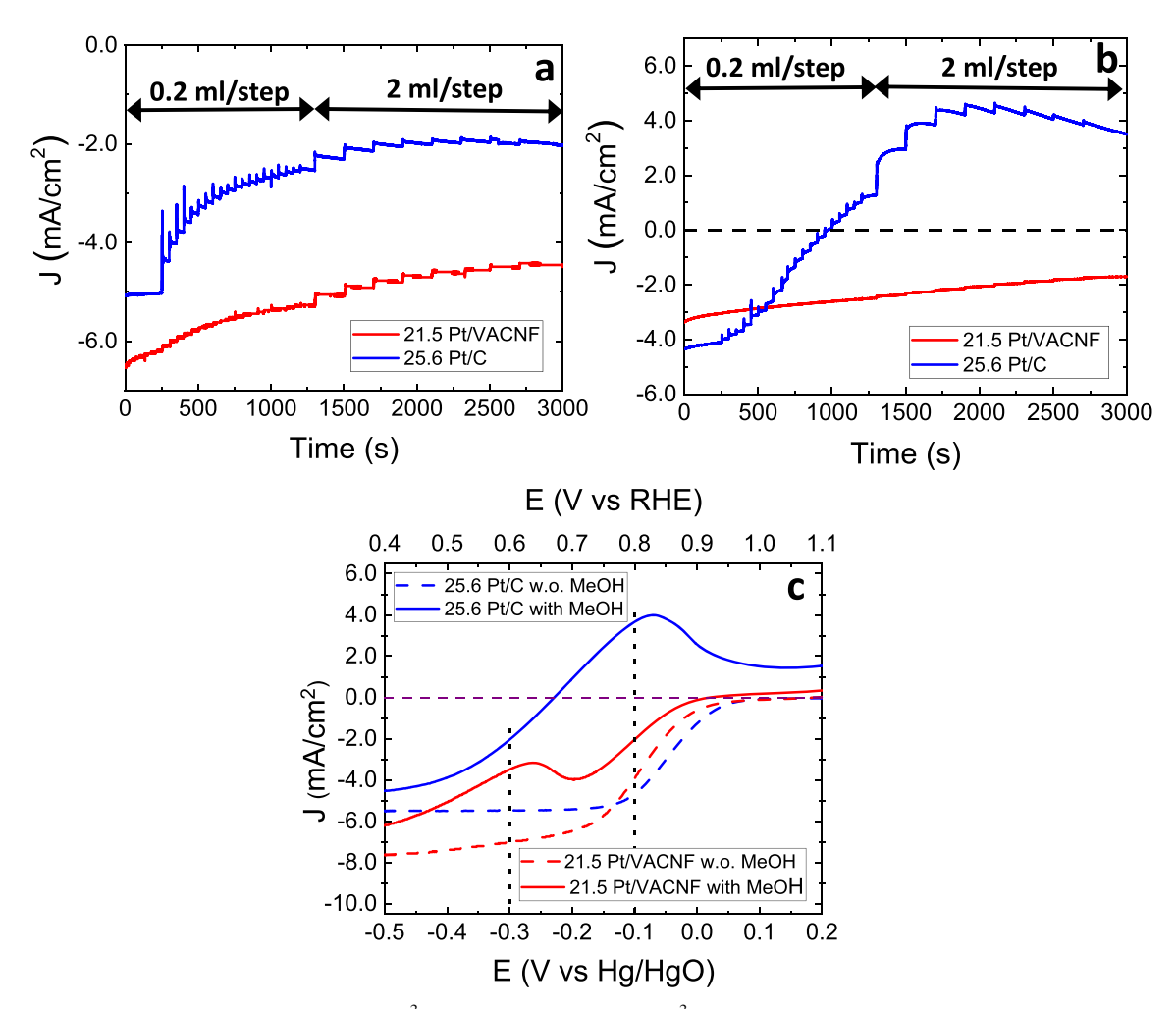


Figure 6. Amperometric *j-t* curves of Pt/C (25.6 μ g cm⁻²) and Pt/VACNF (21.5 μ g cm⁻²) recorded at 1,600 rpm in O₂-saturated 0.10 M KOH solution with successive addition of 3.0 M methanol to give the final concentration of 0.75 M at the potential of (a) -0.3 V (vs Hg/HgO) and (b) -0.1 V (vs Hg/HgO); (c) LSV curves recorded at a scan rate of 10 mV s⁻¹ and 1,600 rpm in 0.10 M KOH with and without the presence of 0.75 M MeOH for Pt/C (25.6 μ g cm⁻²) and Pt/VACNF (21.5 μ g cm⁻²). The purple dash lines mark the zero current density and black dot lines mark the potential at which the amperometric *j-t* curve was recorded.

Pt/C. Thus, the Pt/VACNF catalysts show higher selectivity for ORR.

Resistance to CO poisoning.—An ideal catalyst should be completely immune to CO poisoning or able to rapidly recover the activity after desorbing CO. This has been evaluated for the Pt/ VACNF catalyst (at 10.8 and 21.5 μ g cm⁻² Pt loadings) in comparison with the commercial Pt/C catalyst (at 12.8 and 25.6 μ g cm⁻² Pt loadings) by recording LSVs at 1600 rpm in 0.10 M KOH solution at three different conditions: (1) the initial system purged with pure O₂ for standard ORR; (2) the system purged with 10% CO mixed in 90% O₂ for poisoning effects; and (3) the system re-purged with pure O2 for the recovering capability. Steps (2) and (3) are alternately repeated 5 times. As shown in Figs. 7a and 7b, it is clear that the ORR limiting current density drops when the system is first exposed to CO and it completely recovers to the initial performance after re-purging with pure O_2 for both the 25.6 μg cm⁻² Pt/C catalyst and the 21.5 μg cm⁻² Pt/VACNF catalyst. But after the 5th purge with 10% CO, the limiting current density of the Pt/C catalyst drops much more and is not completely recovered after re-purge with O₂. In contrast, the limiting current of the Pt/VACNF catalyst in 5th CO purge drops by about the same amount as in the first CO purge and is nearly fully recovered when re-purged with O₂. Fig. 7c presents the change in half-wave potential

between the initial LSV curve and LSV curves recorded at different purging conditions. After the fifth trial of CO poisoning, the $E_{1/2}$ has only a small shift of -4 mV in the Pt/VACNF catalyst whereas it is -40 mV in the Pt/C catalyst. Fig. S21 shows a similar behavior observed at lower Pt loading with 12.8 $\mu g \ cm^{-2}$ Pt/C and $10.8 \ \mu g \ cm^{-2}$ Pt/VACNF during the CO and pure O_2 purging cycles. These results indicate that Pt/VACNF has clearly a better recovery capability from CO poisoning than the commercial Pt/C catalysts and it can be attributed to either the stronger O_2 adsorption or the presence of O species on the VACNF-supported Pt NPs which help to remove CO.

Conclusions

In summary, the VACNF array grown by PECVD has been demonstrated as a unique 3D architecture to support ion-sputtered Pt catalysts for ORR. The linear sweep voltammetry of ORR based on such 3D structures on RDE has been found to deviate from the Levich equation. The raised edge and the roughness at the top surface of the nanostructured VACNF array alter the hydrodynamic conditions and the stagnant diffusion layer thickness, resulting in a slanted ORR curve and an increased limiting current density in the Pt/VACNF system. Despite this complication, useful information can be extracted from the RDE measurements. The half-wave

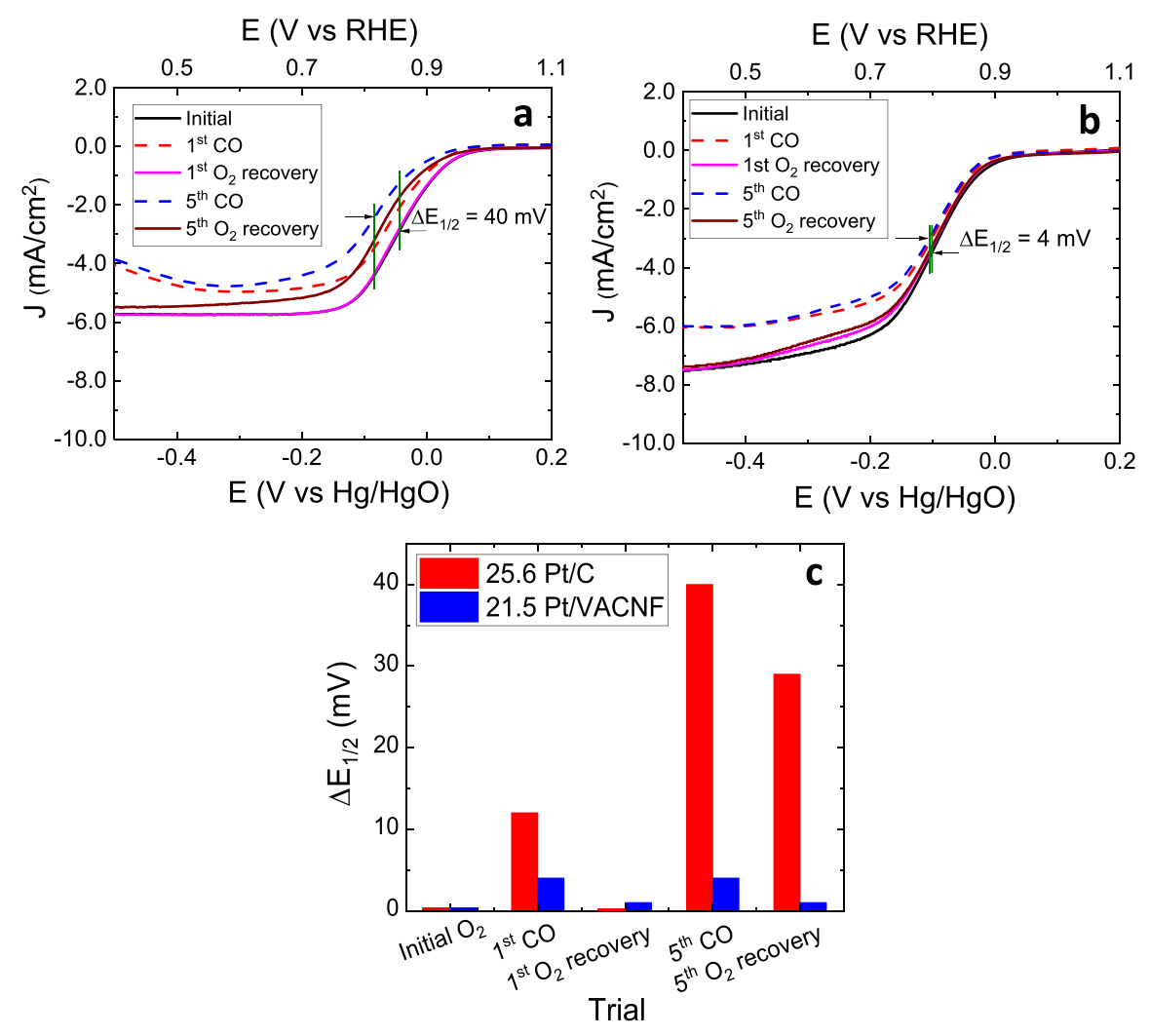


Figure 7. LSV curves recorded at a scan rate of 10 mV s⁻¹ and 1,600 rpm in 0.10 M KOH initially purged with pure O_2 , then with 10 % CO and 90% O_2 (CO poisoning), and re-purged with pure O_2 (O_2 recovery) for (a) Pt/C (25.6 μ g cm⁻²) and (b) Pt/VACNF (21.5 μ g cm⁻²). (The initial and 1st O_2 recovery LSV curve is overlapped in Fig. 7a). The purging sequence was repeated 5 times and only the data from the first and fifth sets are presented. (c) Plot of the negative shift of the half-wave potential ($\Delta E_{1/2}$) vs the different purging conditions.

potential of the Pt/VACNF catalysts is comparable to the benchmark commercial Pt/C catalyst at similar Pt loadings following a 4-e ORR pathway. DFT calculations have validated the strong binding of Pt atoms with the graphitic edge sites in Pt/VACNF catalysts. Based on these models, we have concluded that ORR proceeds via a 2-e pathway on bare VACNFs and a 4-e pathway on Pt/VACNF, respectively. The Pt/VACNF catalyst has shown better durability in accelerated stress tests than the commercial Pt/C catalyst at similar loading. Furthermore, the Pt/VACNF catalysts have shown enhanced tolerance to methanol oxidation. The ORR is the dominant reaction in the full potential range with the Pt/VACNF catalysts in the presence of 0.75 M methanol while methanol oxidation surpasses ORR above -0.2 V (vs Hg/HgO) with the commercial Pt/C catalyst. The Pt/VACNF system has also shown improved capability to recover from CO poisoning. These results provide new insights into the critical roles of 3D nanostructured carbon supports and their graphitic microstructures on the fundamental electrocatalytic properties of the catalyst.

Acknowledgments

This work was supported by the National Science Foundation grant CBET-1703263. We thank Dr. Prem Thapa from the University of Kansas for helping with TEM images and elemental mapping, and Dr. Morgan Anderson for helping with FESEM images. The computation work in this project was performed on the Beocat Research Cluster at Kansas State University, which is funded in part by NSF grants CHE-1726332, CNS-1006860, EPS-1006860, EPS-0919443, National Energy Research Scientific Computing Centre (NERSC) under the contract DEAC02-05CH11231, and the Extreme Science and Engineering Discovery Environment (XSEDE) supported by the National Science Foundation grant number ACI-1548562.

ORCID

Ayyappan Elangovan https://orcid.org/0000-0002-0985-2475 Jiayi Xu https://orcid.org/0000-0003-1763-6251 Bin Liu https://orcid.org/0000-0001-7890-7612 Jun Li https://orcid.org/0000-0002-3689-8946

References

- 1. J.-H. Wee, Renew. Sust. Energy Rev., 11, 1720 (2007).
- 2. A. Rabis, P. Rodriguez, and T. J. Schmidt, ACS Catal., 2, 864 (2012).
- 3. E. Antolini, *Appl. Catal. B: Environ.*, **88**, 1 (2009).
- 4. A. A. Gewirth and M. S. Thorum, *Inorg. Chem.*, 49, 3557 (2010).
- 5. A. Morozan, B. Jousselme, and S. Palacin, Energy Environ. Sci., 4, 1238 (2011).
- Z. Peng and H. Yang, *Nano Today*, **4**, 143 (2009).
- 7. K. Gong, F. Du, Z. Xia, M. Durstock, and L. Dai, *Science*, **323**, 760 (2009).
- 8. C. Koenigsmann and S. S. Wong, *ACS Catal.*, *3*, 2031 (2013). 9. A. K. Shukla and R. K. Raman, *Annu. Rev. Mater. Res.*, *33*, 155 (2003).
- 10. M. K. Debe, *Nature*, **486**, 43 (2012).
- 11. X. X. Wang, M. T. Swihart, and G. Wu, Nat. Catal., 2, 578 (2019).
- 12. Y. Nie, L. Li, and Z. Wei, Chem. Soc. Rev., 44, 2168 (2015).
- 13. X. Yu and S. Ye, J. Power Sources, 172, 133 (2007).
- 14. X. Yu and S. Ye, J. Power Sources, 172, 145 (2007).
- 15. M. H. Seo, S. M. Choi, H. J. Kim, and W. B. Kim, Electrochem. Commun., 13, 182
- 16. C. Zhu and S. Dong, Nanoscale, 5, 1753 (2013).
- 17. Y. Shao, S. Zhang, C. Wang, Z. Nie, J. Liu, Y. Wang, and Y. Lin, J. Power Sources, **195**, 4600 (2010).
- 18. H. Tang, J. H. Chen, Z. P. Huang, D. Z. Wang, Z. F. Ren, L. H. Nie, Y. F. Kuang, and S. Z. Yao, Carbon, 42, 191 (2004).

- 19. D.-W. Wang and D. Su, Energy Environ. Sci., 7, 576 (2014).
- 20. C. A. Bessel, K. Laubernds, N. M. Rodriguez, and R. T. K. Baker, J. Phys. Chem. B, 105, 1115 (2001).
- 21. K. Lee, J. Zhang, H. Wang, and D. P. Wilkinson, J. Appl. Electrochem., 36, 507 (2006).
- 22. W. Li, M. Waje, Z. Chen, P. Larsen, and Y. Yan, Carbon, 48, 995 (2010).
- 23. H. T. Chung, J. H. Won, and P. Zelenay, Nat. Commun., 4, 1922 (2013).
- 24. Y.-J. Wang, N. Zhao, B. Fang, H. Li, X. T. Bi, and H. Wang, Chem. Rev., 115, 3433 (2015).
- 25. A. Kongkanand, S. Kuwabata, G. Girishkumar, and P. Kamat, Langmuir, 22, 2392 (2006).
- 26. M. M. Shaijumon, S. Ramaprabhu, and N. Rajalakshmi, Appl. Phys. Lett., 88, 253105 (2006).
- 27. M. K. Debe, A. K. Schmoeckel, G. D. Vernstrom, and R. Atanasoski, J. Power Sources, 161, 1002 (2006).

- M. K. Debe et al., *J. Electrochem. Soc.*, **158**, B910 (2011).
 M. K. Debe, *ECS Trans.*, **45**, 47 (2012).
 Z. Q. Tian et al., *Adv. Energy Mater.*, **1**, 1205 (2011).
 R. H. Wakabayashi, H. Paik, M. J. Murphy, D. G. Schlom, M. Brützam, R. Uecker, R. B. van Dover, F. J. DiSalvo, and H. D. Abruña, *J. Electrochem. Soc.*, **164**, H1154 (2017).
- 32. A. V. Melechko, V. I. Merkulov, T. E. McKnight, M. A. Guillorn, K. L. Klein, D. H. Lowndes, and M. L. Simpson, J. Appl. Phys., 97, 041301 (2005).
- 33. B. A. Cruden, A. M. Cassell, Q. Ye, and M. Meyyappan, J. Appl. Phys., 94, 4070
- 34. J. Li and G. P. Pandey, Annu. Rev. Phys. Chem., 66, 331 (2015).
- 35. E. J. Biddinger and U. S. Ozkan, J. Phys. Chem. C, 114, 15306 (2010).
- 36. C. Kim, Y. J. Kim, Y. A. Kim, T. Yanagisawa, K. C. Park, M. Endo, and M.
- S. Dresselhaus, *J. App. Phys.*, **96**, 5903 (2004).

 37. M. Endo, Y. A. Kim, M. Ezaka, K. Osada, T. Yanagisawa, T. Hayashi, M. Terrones, and M. S. Dresselhaus, Nano Lett., 3, 723 (2003).
- 38. J. Liu, J. Essner, and J. Li, Chem. Mater., 22, 5022 (2010).
- 39. Z.-M. Zhou, Z.-G. Shao, X.-P. Qin, X.-G. Chen, Z.-D. Wei, and B.-L. Yi, Int. J. Hydrogen Energy, 35, 1719 (2010).
- 40. G. Kresse and J. Furthmüller, Phys. Rev. B, 54, 11169 (1996).
- 41. J. P. Perdew, K. Burke, and M. Ernzerhof, Phys. Rev. Lett., 77, 3865 (1996).
- 42. P. E. Blöchl, Phys. Rev. B, 50, 17953 (1994).
- 43. H. J. Monkhorst and J. D. Pack, *Phys. Rev. B*, 13, 5188 (1976).
- 44. N. Ooi, A. Rairkar, and J. B. Adams, Carbon, 44, 231 (2006).
- 45. S. Grimme, J. Antony, S. Ehrlich, and H. Krieg, J. Chem. Phys., 132, 154104 (2010).
- 46. Y. A. Zhu, Z. J. Sui, T. J. Zhao, Y. C. Dai, Z. M. Cheng, and W. K. Yuan, Carbon, 43, 1694 (2005)
- 47. X. Hou, Q. Hu, P. Zhang, and J. Mi, Chem. Phys. Lett., 663, 123 (2016).
- 48. S. Wang, E. Iyyamperumal, A. Roy, Y. Xue, D. Yu, and L. Dai, Angew. Chem., 50, 11756 (2011).
- 49. M. E. Scofield, H. Liu, and S. S. Wong, Chem. Soc. Rev., 44, 5836 (2015).
- 50. X. Cai, B. Y. Xia, J. Franklin, B. Li, X. Wang, Z. Wang, L. Chen, J. Lin, L. Lai, and Z. Shen, J. Mater. Chem. A, 5, 2488 (2017).
- 51. T. E. Dinan, M. Matlosz, and D. Landolt, J. Electrochem. Soc., 138, 2947 (1991).
- Y. Garsany, O. A. Baturina, K. E. Swider-Lyons, and S. S. Kocha, Anal. Chem., 82, 6321 (2010).
- 53. A. J. Bard and L. R. Faulkner, Electrochemical Methods: Fundamentals and Applications (Wiley, New York) (1980).
- 54. J. Masa, C. Batchelor-McAuley, W. Schuhmann, and R. G. Compton, *Nano Res.*, 7, 71 (2014).
- 55. D. Shin, B. Jeong, M. Choun, J. D. Ocon, and J. Lee, RSC Adv., 5, 1571 (2015).
- 56. S. Liu, M. G. White, and P. Liu, J. Phys. Chem. C, 120, 15288 (2016).
- 57. J. K. Nørskov, J. Rossmeisl, A. Logadottir, L. Lindqvist, J. R. Kitchin, T. Bligaard, and H. Jónsson, J. Phys. Chem. B, 108, 17886 (2004).
- 58. R. Rizo, E. Herrero, and J. M. Feliu, Phys. Chem. Chem. Phys., 15, 15416 (2013).
- 59. J. Xu and B. Liu, Appl. Surf. Sci., 500, 144020 (2020).
- 60. C. H. Choi, H.-K. Lim, M. W. Chung, J. C. Park, H. Shin, H. Kim, and S. I. Woo, J. Am. Chem. Soc., 136, 9070 (2014).
- 61. N. Shan, M. Zhou, M. K. Hanchett, J. Chen, and B. Liu, Mol. Simul., 43, 861 (2017).
- 62. J. A. Dean, Lange's Handbook of Chemistry (McGraw-Hill, New York) (1985).
- 63. H. Cheng, Y.-A. Zhu, D. Chen, P.-O. Åstrand, P. Li, Z. Qi, and X.-G. Zhou, J. Phys. Chem. C, 118, 23711 (2014).
- 64. H.-Y. Cheng, Y.-A. Zhu, P.-O. Åstrand, D. Chen, P. Li, and X.-G. Zhou, J. Phys. Chem. C, 117, 14261 (2013).